

Lattice-distortion couplings in antiferroelectric perovskite AgNbO_3 and comparison with PbZrO_3

Huazhang Zhang,^{1,2,*} Konstantin Shapovalov,¹ Safari Amisi,^{1,3} and Philippe Ghosez^{1,†}

¹*Theoretical Materials Physics, Q-MAT,*

Université de Liège, B-4000 Sart-Tilman, Belgium

²*Department of Physics, School of Science, Wuhan University of Technology,
Wuhan 430070, People's Republic of China*

³*Laboratoire de Physique des Solides et des Interfaces,
Institut Supérieur Pédagogique de Bukavu, Democratic Republic of the Congo*

(Dated: August 6, 2024)

Abstract

Lead-free antiferroelectric perovskite AgNbO_3 is nowadays attracting extensive research interests due to its promising applications in energy storage. Although great progress has been made in optimizing the material performance, fundamental questions remain regarding the mechanism stabilizing the antiferroelectric $Pbcm$ phase. Here, combining structural symmetry analysis and first-principles calculations, we identified crucial anharmonic couplings of oxygen octahedra rotations and cation antipolar motions which contribute significantly to lowering the energy of the $Pbcm$ phase. The stabilization of this phase shows close similarities with the stabilization of the $Pbam$ phase in PbZrO_3 except that in AgNbO_3 the octahedra rotations are the primary distortions while the antipolar cation motions appear to be secondary. The appearance and significant amplitude of the latter are explained from the combination of hybrid-improper and triggered mechanisms.

Keywords: Antiferroelectricity; silver niobate; lead zirconate; lattice-distortion coupling

* Corresponding author: hzhang@uliege.be

† Corresponding author: philippe.ghosez@uliege.be

I. INTRODUCTION

Antiferroelectric (AFE) materials exhibit characteristic double hysteresis loops, making them attractive for a wide range of applications [1–6]. Among the limited number of perovskite antiferroelectric oxides, AgNbO_3 (ANO) has attracted a lot of research interest because it is lead-free and can exhibit large polarization under electric field ($52 \mu\text{C}/\text{cm}^2$ at $220 \text{ kV}/\text{cm}$ [7]). Recently, extensive studies have focused on the energy storage properties of ANO-based materials and remarkably high energy storage density has been achieved [8–13]. The excellent energy storage performance of ANO is closely related to its AFE property, which involves a reversible phase transition between nonpolar AFE state and a highly polarized ferroelectric (FE) state upon application and removal of an electric field. Understanding the mechanism behind the AFE properties of ANO and identifying the key interactions stabilizing the AFE state are fundamental and meaningful topics, which can provide valuable guidance for the further optimization of its properties.

The exact structure and the AFE nature of ANO are currently subjects of ongoing discussion. In fact, controversies exist regarding its complex series of phase transitions [14–19]. According to the X-ray and neutron diffraction reported by Sciau *et al.* [17], the phase sequence of ANO from high-temperature to low-temperature is: cubic C phase ($Pm\bar{3}m$, above 852 K), tetragonal T phase ($P4/mbm$, $660 \sim 852 \text{ K}$), orthorhombic O phase ($Cmcm$, $626 \sim 660 \text{ K}$), and orthorhombic M phase ($Pbcm$, below 626 K). Although dielectric measurements suggested that there may be several different M phases [13–15], Sciau’s results showed that the average structures of all these possible low-temperature M phases share the same $Pbcm$ space group [17]. The $Pbcm$ structure is centrosymmetric, in line with its AFE property. However, it was also noted that ANO exhibits a weak remanence on the polarization hysteresis loops [13, 20]. This phenomenon may be caused by various reasons, such as cation disordering, polar clusters, or defects [13, 18, 21]. A previous structural study also suggested that a polar $Pmc2_1$ structure might be the low-temperature phase of ANO [22], but the subsequent density functional theory (DFT) calculations have shown that this $Pmc2_1$ structure is not stable [23]. Instead, the $Pbcm$ phase remains the lowest energy phase in literature and is free of any dynamical instability, including under negative pressure [23], indicating that it is the most probable antiferroelectric phase of ANO.

The emergence of a $Pbcm$ phase is rather uncommon in perovskite oxides [24, 25]. The

most common structure for perovskites with small tolerance factors ($t < 1$) is $Pnma$ [26], a phase which is favored by a trilinear coupling between cation antipolar motions and in-phase and antiphase oxygen octahedra rotations [27]. Then, among antiferroelectrics, the phase that attracted the most attention is $Pbam$, as seen in, e.g., the prototypical antiferroelectric $PbZrO_3$ (PZO), where it is stabilized by a trilinear coupling between cation displacements, oxygen octahedra rotations and their modulations [28–31]. In ANO, however, the stabilization mechanism of the $Pbcm$ antiferroelectric state has not been fully clarified.

In this study, we investigate the stabilization mechanism of the $Pbcm$ antiferroelectric state through structural symmetry analysis and first-principles calculations, aiming at understanding why such an unusual phase in perovskites can exhibit a low energy in ANO. We identify the combination of trilinear and cooperative biquadratic couplings between cation antipolar motions and oxygen octahedra rotations as the key contributions to the energy lowering of the $Pbcm$ phase. We also conduct a comparison between ANO and the prototypical antiferroelectric PZO. Our findings suggest a combination of hybrid-improper and triggered mechanisms for the appearance of the cation antipolar motions in ANO.

II. CALCULATION DETAILS

First-principles DFT calculations were performed using the ABINIT package [32–35] with the plane-wave-pseudopotential approach. We employed the generalized gradient approximation (GGA) with the revised Perdew-Burke-Enzerh parameterization for solids (PBEsol) [36] and optimized norm-conserving pseudopotentials from the PseudoDojo server [37, 38]. The valence electron configurations are $4s^2 4p^6 4d^{10} 5s^1$ for Ag, $4s^2 4p^6 4d^4 5s^1$ for Nb, $5s^2 5p^6 5d^{10} 6s^2 6p^2$ for Pb, $4s^2 4p^6 4d^2 5s^2$ for Zr, and $2s^2 2p^4$ for O. For comparison, we also checked some results using the local density approximation (LDA) functional [39]. The energy cutoff for the plane-wave expansion was 50 Ha for ANO and 60 Ha for PZO. The k -point grids were equivalent to or denser than $6 \times 6 \times 6$ grid for the five-atom cubic perovskite. The electronic self-consistent cycles were considered to be converged until the potential residual is smaller than 10^{-18} Ha. Structural relaxations were performed based on the Broyden-Fletcher-Goldfarb-Shanno minimization algorithm, using the convergence criteria of 10^{-6} Ha/Bohr for the forces and 10^{-8} Ha/Bohr³ for the stresses. The phonon dispersions were calculated according to density functional perturbation theory as imple-

mented in ABINIT and analyzed with the ANADDB program [40]. The symmetry-adapted lattice-distortion modes were analyzed using ISODISTORT [41]. The energy expansions were build with the help of INVARIANTS [42].

III. MODE COUPLINGS IN ANO

The structural parameters of ANO in its $Pbcm$ phase are reported in Table I, where we compare the results of our GGA-PBEsol and LDA calculations with the experimental data from low-temperature measurements in literature [17]. The GGA-PBEsol calculated lattice parameters show very good agreement with the experimental values, with discrepancies less than 0.5%, while the LDA tends to underestimate the lattice constants. It is therefore expected that the GGA-PBEsol functional is more accurate in capturing the structural characteristics of ANO.

Table I. Lattice parameters (\AA) and atomic positions (reduced coordinates) of ANO in the orthorhombic $Pbcm$ phase. The x, y, z coordinates are in the direction of orthorhombic axes a, b, c , respectively.

Lattice parameter (\AA)	GGA-PBEsol			LDA			Exp. (1.5 K) [17]		
	a	b	c	a	b	c	a	b	c
Error (%)	-0.40	-0.09	-0.38	-1.83	-1.26	-1.12			
	x	y	z	x	y	z	x	y	z
Ag1 (4c)	0.7423	0.25	0	0.7439	0.25	0	0.7449	0.25	0
Ag2 (4d)	0.7369	0.2210	0.25	0.7378	0.2226	0.25	0.7420	0.2211	0.25
Nb (8e)	0.2436	0.2210	0.1250	0.2445	0.2270	0.1250	0.2436	0.2212	0.1249
O1 (8e)	-0.0438	0.0445	0.1082	-0.0473	0.0479	0.1067	-0.0348	0.0371	0.1098
O2 (8e)	0.5445	0.4620	0.1417	0.5462	0.4603	0.1436	0.5360	0.4689	0.1396
O3 (4c)	0.3167	0.25	0	0.3234	0.25	0	0.3109	0.25	0
O4 (4d)	0.1872	0.2752	0.25	0.1794	0.2787	0.25	0.1944	0.2678	0.25

As shown in Fig. 1(a), the unit cell of the $Pbcm$ phase can be viewed as a $\sqrt{2} \times \sqrt{2} \times 4$ multiple of the five-atom perovskite elemental unit cell, with the translational vectors $a, b,$

c directed along the pseudocubic $[1\bar{1}0]$, $[110]$, $[001]$ directions. By symmetry analysis, the atomic distortion of the $Pbcm$ phase with respect to the cubic reference structure can be decomposed into symmetry-adapted lattice-distortion modes of this reference [Fig. 1(b) and Table II]. The dominating modes are [Fig. 1(a)]: (1) R_5^- mode, the rotations of oxygen octahedra around the b -axis that correspond to $a^-a^-c^0$ rotation pattern in Glazer's notation [43]; (2) T_2 mode, a complex octahedra rotation pattern alternating between in-phase and antiphase rotations around the c -axis that we label hereafter as the $a^0a^0c^{+/-}$ rotation pattern; (3) Δ_5 mode, primarily the antipolar motions of the cations Ag and Nb in the direction of b -axis; (4) M_5^- mode, the antipolar motions of Ag and Nb in the direction of a -axis. The above four modes account for 48.88%, 41.13%, 9.02% and 0.86% of the total lattice distortion, respectively, while the remaining modes account for the remaining 0.11%. The fact that most of the distortions are associated to the oxygen octahedra rotations is consistent with the small tolerance factor of ANO ($t = 0.965$) since octahedra rotations are typical in perovskites with tolerance factor smaller than 1 [26].

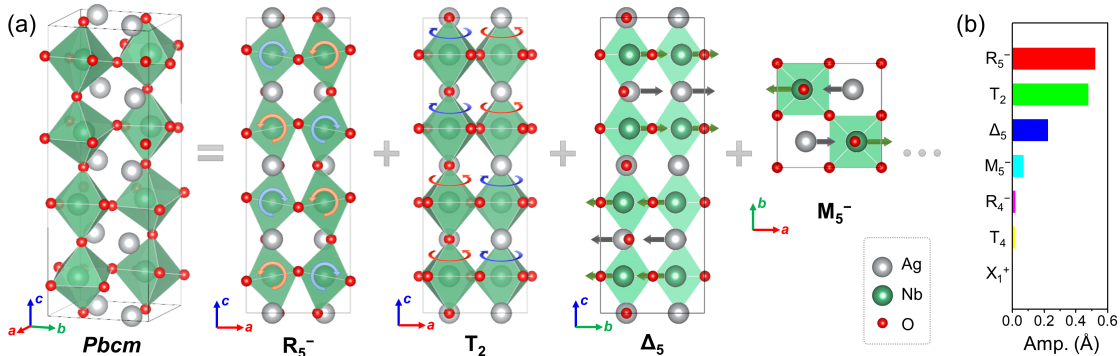


Figure 1. Structure and symmetry-adapted lattice-distortion modes (respect to the cubic reference structure) of ANO in the $Pbcm$ phase. (a) Schematics of the $Pbcm$ crystal structure and the dominant modes of the cubic reference structure giving rise to the $Pbcm$ phase. (b) Mode amplitudes in the $Pbcm$ structure, respect to the cubic reference, as optimized with the GGA-PBEsol functional.

We can gain more insight into the stabilization mechanism of the $Pbcm$ phase by investigating the structural and energetic relationships among different phases of ANO, paying specific attention to the phases with different oxygen octahedra rotations. In each calculation, we introduce octahedra rotations to the prototypical cubic $Pm\bar{3}m$ phase and relax the atomic distortions and lattice parameters while preserving the symmetry of the distortions in

Table II. Symmetry-adapted lattice-distortion mode decomposition of the $Pbcm$ phase of ANO. The structure is obtained by relaxing fully the atomic positions and lattice parameters using GGA-PBEsol functional. The mode amplitudes are reported in the so-called “parent-cell-normalized” values of ISODISTORT.

	R_5^-	T_2	Δ_5	M_5^-	R_4^-	T_4	X_1^+
Amplitude (Å)	0.5202	0.4772	0.2235	0.0691	0.0177	0.0164	0.0005
Percentage (%)	48.88	41.13	9.02	0.86	0.06	0.05	< 0.01

order to obtain the corresponding metastable phase. Specifically, we consider three types of octahedra rotation patterns around the c -axis, namely $a^0a^0c^+$, $a^0a^0c^{+/-}$, and $a^0a^0c^-$, which are corresponding to the M (1/2, 1/2, 0), T (1/2, 1/2, 1/4), and R (1/2, 1/2, 1/2) points in reciprocal space, respectively, as well as the octahedra rotations around b -axis corresponding to $a^-a^-c^0$ rotation pattern in Glazer’s notation.

Figure 2(a) schematically illustrates the structural and energetic relationships among various phases. When only one rotation around the c -axis is present, the three phases $P4/mbm$ ($a^0a^0c^+$), $I4/mcm$ ($a^0a^0c^{+/-}$) and $I4/mcm$ ($a^0a^0c^-$) are very close in energy [Fig. 2(a)], which is consistent with the almost non-dispersive nature of the lowest $M - T - R$ branch of the phonon dispersion curve calculated in the cubic phase [Fig. 2(b)]. This implies that the rotations of oxygen octahedra, while naturally strongly correlated within the planes perpendicular to the rotation axis c , are weakly correlated between adjacent planes. Consequently, the rotations between adjacent planes being either in-phase or antiphase do not result in significant energy differences.

Interestingly, when the octahedra rotations around the c -axis coexist with the $a^-a^-c^0$ rotations, we find that the energies of the relaxed $Pbnm$ ($a^-a^-c^+$, equivalent to $Pnma$ but hereafter will be referred to it as $Pbnm$ to keep consistency with the crystallographic coordinate system), $Pbcm$ ($a^-a^-c^{+/-}$) and $R\bar{3}c$ ($a^-a^-a^-$) phases are no longer so close to each other. In particular, the energy lowering from $I4/mcm$ ($a^0a^0c^{+/-}$) to $Pbcm$ ($a^-a^-c^{+/-}$) is notably larger than in the other two cases [i.e. from $P4/mbm$ ($a^0a^0c^+$) to $Pbnm$ ($a^-a^-c^+$), and from $I4/mcm$ ($a^0a^0c^-$) to $R\bar{3}c$ ($a^-a^-a^-$)]. As we will show below, such comparatively larger energy lowering is caused by condensation of additional non-polar modes trilinearly coupled to the octahedra rotations. In addition to this, $R\bar{3}c$ phase allows a further lowering

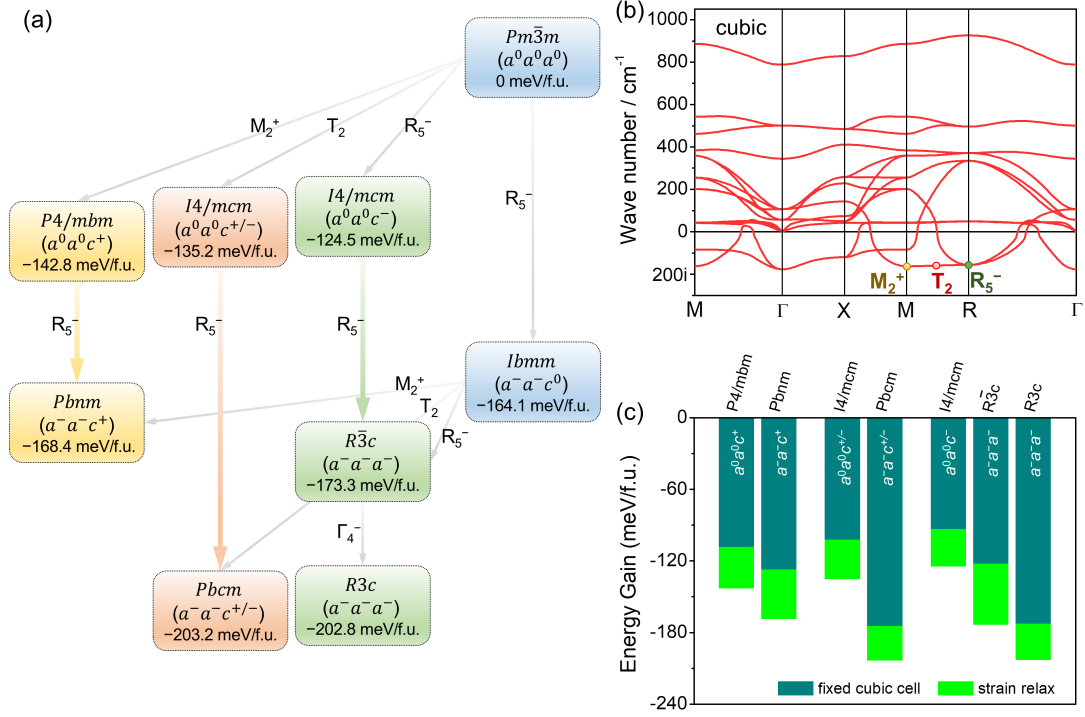


Figure 2. (a) Structural and energetic relationships of various metastable phases. (b) Phonon dispersion curves of ANO in the cubic parent phase. (c) Comparisons of the energies of the metastable phases (respect to the cubic phase taken as reference) with either fixed lattice parameters of the cubic parent phase or fully relaxed lattice parameters. The notations for orthorhombic space groups $Pbnm$ and $Ibmm$ are chosen to keep consistency with the crystallographic coordinate system of this work, but it should be noted that these space groups are commonly referred to as $Pnma$ and $Imma$ in the literature, respectively, as they are equivalent.

of its symmetry towards $R\bar{3}c$ by introducing a polar mode Γ_4^- along the total rotation axis in the $a^- a^- a^-$ pattern (pseudocubic [111] direction), resulting in a large energy lowering. Nevertheless, the energy of the $R\bar{3}c$ phase is still a bit higher than that of the $Pbcm$ phase.

The impact of strain relaxation is examined in Fig. 2(c), where, in addition to the above results, we report the energies of the phases obtained at fixed lattice parameters of the cubic parent phase. It can be seen that fixing the lattice parameters does not qualitatively change the energetics of the phases: the energy reduction from $I4/mcm$ ($a^0 a^0 c^{+/-}$) to $Pbcm$ ($a^- a^- c^{+/-}$) is as pronounced as with strain relaxation, with the $Pbcm$ phase still slightly below the $R\bar{3}c$ phase in energy. This rules out the strain-phonon coupling to be a dominant

factor for stabilizing the *Pbcm* phase.

We then turn to analyze in more details how the lattice-distortion modes are coupled in ANO. We will mainly focus on the *Pbcm* phase and take the *Pbnm* and *R3c* phases for comparisons. We will adopt Landau-type energy expansion in terms of symmetry-adapted lattice-distortion modes for the understanding of the mode couplings, and neglect strain relaxation which does not play a dominant role.

For the *Pbcm* phase, we consider the aforementioned four dominating modes, i.e. R_5^- , T_2 , Δ_5 and M_5^- . Taking these modes as order parameters and restricting to the lowest necessary fourth order, the Landau energy expansion for the *Pbcm* phase is written as

$$\begin{aligned}
E_{Pbcm} = & E_{\text{cubic}} + A_R Q_R^2 + B_R Q_R^4 + A_T Q_T^2 + B_T Q_T^4 + A_\Delta Q_\Delta^2 + B_\Delta Q_\Delta^4 \\
& + A_{M'} Q_{M'}^2 + C_{RT\Delta} Q_R Q_T Q_\Delta + C_{T\Delta M'} Q_T Q_\Delta Q_{M'} \\
& + D_{RT} Q_R^2 Q_T^2 + D_{R\Delta} Q_R^2 Q_\Delta^2 + D_{T\Delta} Q_T^2 Q_\Delta^2,
\end{aligned} \tag{1}$$

where E_{cubic} is the energy of the cubic reference structure, Q_R , Q_T , Q_Δ and $Q_{M'}$ are the amplitudes of the R_5^- , T_2 , Δ_5 and M_5^- modes, respectively, and the A , B , C , D parameters are the coefficients of the energy expression, with subscript indicating the associated modes. For comparisons, we also write the energy expansions for the *Pbnm* phase

$$\begin{aligned}
E_{Pbnm} = & E_{\text{cubic}} + A_R Q_R^2 + B_R Q_R^4 + A_M Q_M^2 + B_M Q_M^4 + A_X Q_X^2 \\
& + C_{RMX} Q_R Q_M Q_X + D_{RM} Q_R^2 Q_M^2 + D_{RX} Q_R^2 Q_X^2 + D_{MX} Q_M^2 Q_X^2,
\end{aligned} \tag{2}$$

where Q_R , Q_M , and Q_X are the amplitudes of the R_5^- , M_2^+ , and X_5^- dominant modes, respectively, and for the *R3c* phase

$$E_{R3c} = E_{\text{cubic}} + A_{R'} Q_{R'}^2 + B_{R'} Q_{R'}^4 + A_\Gamma Q_\Gamma^2 + B_\Gamma Q_\Gamma^4 + D_{R'\Gamma} Q_{R'}^2 Q_\Gamma^2, \tag{3}$$

where $Q_{R'}$ and Q_Γ are the amplitudes of the R_5^- and Γ_4^- modes, respectively.

To quantify the coefficients in the energy expansions, we constructed first-principles data sets for each of the *Pbcm*, *Pbnm* and *R3c* phases by introducing relevant lattice-distortion modes with different mode amplitudes to the prototypical $Pm\bar{3}m$ cubic phase at fixed cubic lattice parameters, and performed the global least-squares fittings of all the energy data points. For all the three phases, the fitting shows good quality ($R^2 = 0.9975$), indicating that these energy expressions describe well the associated potential energy surfaces. The obtained coefficients are summarized in Table III.

Table III. Fitted coefficients for the Landau energy expansions of the $Pbcm$ [Eq. (1)], $Pbnm$ [Eq. (2)] and $R3c$ [Eq. (3)] phases of ANO at fixed cubic lattice parameters. The coefficients are fitted using the units of energy in meV/f.u. and mode amplitudes in Å. The values in brackets are instead the coefficients fitted using relative mode amplitudes (i.e. with mode amplitudes normalized to 1 in the relaxed structure of each phase), which also correspond to the energy contributions (meV/f.u) of the related terms to the energy lowering of each phase. The mode amplitudes in each phase can be easily derived from the ratio between the coefficients and the corresponding energy contribution in brackets.

Phase	Fitted coefficients (Energy contributions)			
$Pbcm$	$A_R = -670.5$ (-113.9)	$B_R = +976.3$ (+28.2)	$C_{RT\Delta} = -691.8$ (-34.3)	$D_{RT} = +1721.4$ (+85.3)
	$A_T = -682.6$ (-199.2)	$B_T = +1099.1$ (+93.6)	$C_{T\Delta M'} = -4692.4$ (-55.5)	$D_{R\Delta} = -1257.0$ (-10.6)
	$A_\Delta = -443.3$ (-22.0)	$B_\Delta = +21447.7$ (+53.0)		$D_{T\Delta} = -1959.4$ (-28.4)
	$A_{M'} = +2878.0$ (+27.7)			
$Pbnm$	$A_R = -670.5$ (-137.4)	$B_R = +976.3$ (+41.0)	$C_{RMX} = -1443.2$ (-17.3)	$D_{RM} = +1859.9$ (+63.1)
	$A_M = -717.2$ (-118.8)	$B_M = +1151.4$ (+31.6)		$D_{RX} = +1079.9$ (+0.9)
	$A_X = +1547.3$ (+6.6)			$D_{MX} = +1654.3$ (+1.2)
$R3c$	$A_{R'} = -670.5$ (-299.4)	$B_{R'} = +901.3$ (+179.7)		$D_{R'\Gamma} = -2194.2$ (-60.1)
	$A_\Gamma = -768.8$ (-47.1)	$B_\Gamma = +14264.8$ (+53.6)		

It is worth noticing that the energy expansion of the $Pbcm$ phase [Eq. (1)] includes two trilinear coupling terms, i.e. $C_{RT\Delta}Q_RQ_TQ_\Delta$ and $C_{T\Delta M'}Q_TQ_\Delta Q_{M'}$. We plotted in Figs. 3(a, b) the associated energy curves. In Fig. 3(a), it is seen that the antipolar Δ_5^- mode, when condensed alone in the cubic phase, can only give rise to a shallow and symmetric double well. However, combined with the R_5^- and T_2 modes, the energy curve becomes highly asymmetric, highlighting the effect of the trilinear coupling term $C_{RT\Delta}Q_RQ_TQ_\Delta$. In Fig. 3(b), the potential energy curve associated with the M_5^- mode is initially symmetric and single-well shaped when T_2 and Δ_5^- modes are zero. However, when the amplitudes of T_2 and Δ_5^- modes are non-zero, the potential well becomes asymmetric with the bottom of the well shifting to a non-zero amplitude of M_5^- mode. This is a consequence of the trilinear coupling term $C_{T\Delta M'}Q_TQ_\Delta Q_{M'}$.

In the $Pbnm$ phase, there exists a similar trilinear term $C_{RMX}Q_RQ_MQ_X$ [Eq. (2)], which represents the coupling of octahedra rotations R_5^- , M_2^+ , and cation antipolar motion X_5^- . This trilinear coupling has been well-known in literature, as the $Pbnm$ symmetry is the most commonly observed in perovskites [44]. Fig. 3(c) shows the associated energy curves

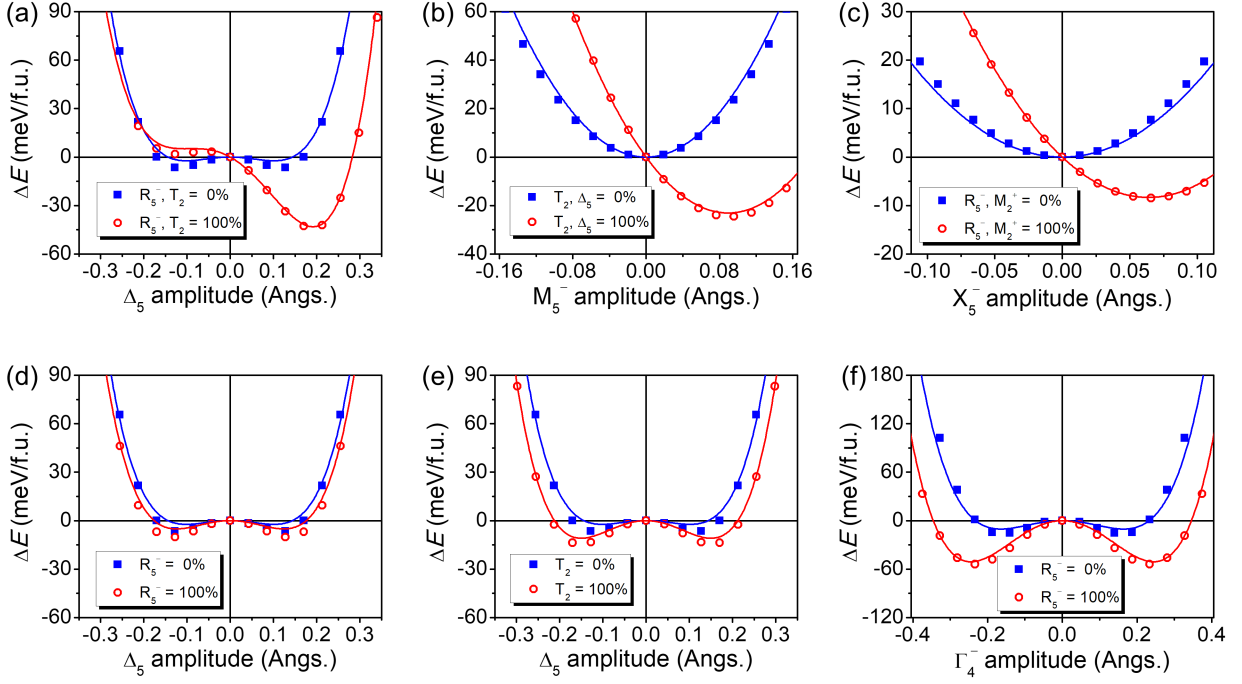


Figure 3. Evolution of the energy of ANO when condensing different symmetry adapted mode in the cubic phase (taken as energy reference) in the absence or eventually in the presence of other modes as indicated by the legends. Mode amplitudes of 100% correspond to the amplitude in the relaxed (a, b, d, e) $Pbcm$, (c) $Pnma$ and (f) $R3c$ phases with cubic lattice parameters.

in ANO. By itself, the X_5^- mode is characterized by a single energy well. The introduction of R_5^- and M_2^+ modes leads to the asymmetric shift of the single well due to the trilinear coupling.

Having a closer look at the $Pbcm$ and $Pbnm$ phases of ANO, one can see similarities between the modes involved in the respective trilinear couplings of R_5^- , T_2 and Δ_5 , and of R_5^- , M_2^+ and X_5^- . The first mode, R_5^- , comprises the same $a^-a^-c^0$ rotations present in both phases; because of this we fixed the coefficients A_R and B_R to have the same value in the energy expansions for the two phases [Eqs. (1, 2)]. The second mode, T_2 in $Pbcm$ and M_2^+ in $Pbnm$, essentially comprises oxygen octahedra rotations around the c -axis, the main difference being the relative signs of the rotations. In the M_2^+ mode, all oxygen octahedra in a c -directed column have the same rotation sign, while in T_2 the octahedra in a c -directed column form a $++--$ rotation pattern. The M_2^+ and T_2 modes having the same mode amplitude show the same absolute rotation angle and have very similar energetics: indeed,

as one can see in Tab. III, A_T and A_M , as well as B_T and B_M have almost identical values, lying within 5% from each other.

The main difference in the energetics comes from the third mode, which is Δ_5 in $Pbcm$ and X_5^- in $Pbnm$. At a first glance, from the point of view of crystalline structure, these modes are very similar: they both consist of b -directed antipolar cation motions manifesting in the same kind of displacement of the Ag cations lying within the same plane normal to the c -axis. In the X_5^- mode, the Ag planes form a $+ -$ displacement pattern, while in the Δ_5 mode they form a $+0-0$ pattern. Interestingly, in the $Pbcm$ phase, the non-zero Ag displacement planes of the Δ_5 mode are centered between the *in-phase* layers of the oxygen octahedral $++--$ rotation pattern of the T_2 mode [Fig. 1(a)], locally reminiscing the distortions observed in the $Pbnm$ phase. This points towards similar origins for the trilinear coupling of R_5^- , T_2 and Δ_5 that we report here and the well-known trilinear coupling of R_5^- , M_2^+ and X_5^- . Despite this similarity, the energy lowering from $I4/mcm$ to $Pbcm$ phase is significantly larger than from $P4/mbm$ to $Pbnm$ [Fig. 2(a)]. One reason for this is that inducing the X_5^- mode by itself costs energy, consistently with the positive sign of its quadratic coefficient in the energy expansion ($A_X > 0$) and by the single-well nature of the related energy in Fig. 3(c). On the contrary, the Δ_5 mode is, by itself, unstable in the cubic phase ($A_\Delta < 0$), as apparent from the double-well energy profile in Fig. 3(a), allowing for larger trilinear-coupling-mediated energy gains.

In addition to the trilinear couplings, the energy expansion of the $Pbcm$ phase [Eq. (1)] also contains three biquadratic coupling terms: $D_{RT}Q_R^2Q_T^2$, $D_{R\Delta}Q_R^2Q_\Delta^2$ and $D_{T\Delta}Q_T^2Q_\Delta^2$. Among them, the latter two have negative coefficients, i.e. $D_{R\Delta} < 0$ and $D_{T\Delta} < 0$ (Table III), revealing the cooperative nature of the biquadratic interactions between R_5^- and Δ_5 [Fig. 3(d)] and between T_2 and Δ_5 [Fig. 3(e)]. In contrast, in $Pbnm$ phase all biquadratic couplings are competitive, with D_{RM} , D_{RX} , $D_{MX} > 0$, which makes another important contribution to the different energy lowering and is ultimately favoring $Pbcm$ over $Pbnm$ in ANO. Interestingly, we also observe a similar cooperative biquadratic coupling $D_{RT}Q_R^2Q_T^2$ in the $R3c$ phase [Eq. (3), Fig. 3(f)]. This cooperative biquadratic coupling in $R3c$ leads to an even more significant energy lowering than the cooperative biquadratic coupling in the $Pbcm$ phase (Table III).

To gain deeper insights on the effects of distinct couplings on the stabilization of the $Pbcm$ phase and to make the above discussion of the couplings more quantitative, we performed

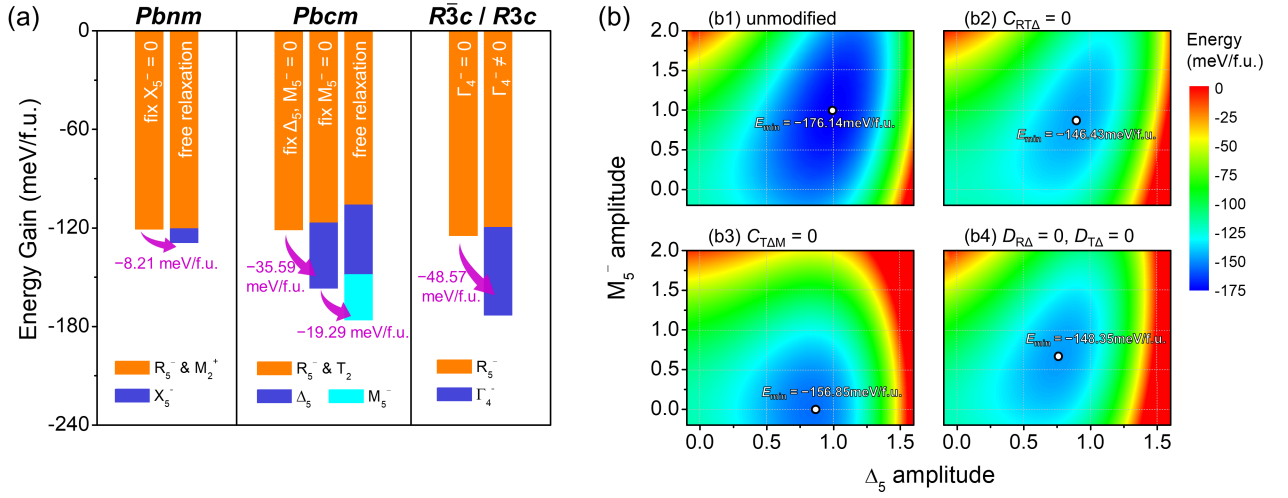


Figure 4. (a) Energy lowerings of *Pbcm*, *Pbnm* and $\bar{R}3c/R3c$ phases with respect to the cubic parent phase when different distortion modes are progressively introduced and relaxed. (b) Effects of “switching off” some specific couplings on the potential energy surfaces of the *Pbcm* phase in terms of the amplitudes of Δ_5 and M_5^- modes. At each point on the plots in (b), the energy value were calculated by relaxing R_5^- and T_2 modes at the fixed Δ_5 and M_5^- amplitudes.

Landau-based calculations where different distortion modes are progressively introduced and relaxed. As shown in Fig. 4(a), when only the octahedra rotation modes are allowed to relax while the polar/antipolar modes are fixed to zero, the *Pbnm*, *Pbcm*, and $\bar{R}3c$ structures exhibit very similar energies, namely -120.9 meV/f.u., -121.3 meV/f.u., and -124.7 meV/f.u., respectively. In this case, the *Pbcm* phase does not show any significant energy advantage over the *Pbnm* and $\bar{R}3c$ phases.

When we further allow the polar/antipolar modes to relax, we find that the *Pbcm* phase acquires a significant energy lowering. As shown in Fig. 4(a), by introducing antipolar Δ_5 and M_5^- modes, the energy of *Pbcm* phase is lowered by 35.59 meV/f.u. and 19.29 meV/f.u., respectively. In comparison, the introduction of antipolar X_5^- mode in the *Pbnm* phase only lowers the energy by 8.21 meV/f.u.. In the $\bar{R}3c$ phase, the condensation of the polar Γ_4^- mode also leads to a significant energy reduction of 48.57 meV/f.u., but the resulting *R3c* phase has an energy still slightly higher than that of the *Pbcm* phase. These results demonstrate the crucial role of the antipolar Δ_5 and M_5^- modes and of their related couplings in stabilizing the *Pbcm* phase.

Table IV. Energy and mode amplitudes of the relaxed $Pbcm$ phase when artificially “switching off” some specific coupling terms. The mode amplitudes are normalized to 1 in the real $Pbcm$ phase (“unmodified” case).

	E_{\min} (meV/f.u.)	R_5^-	T_2	Δ_5	M_5^-
unmodified	-176.14	1.000	1.000	1.000	1.000
$C_{RT\Delta} = 0$	-146.43	0.791	1.011	0.901	0.911
$C_{T\Delta M'} = 0$	-156.85	1.143	0.826	0.839	0.000
$D_{R\Delta} = 0$	-167.29	0.862	1.038	0.964	1.001
$D_{T\Delta} = 0$	-156.53	1.145	0.823	0.836	0.688
$C_{RT\Delta} = 0, C_{T\Delta M'} = 0$	-133.19	1.122	0.751	0.697	0.000
$D_{R\Delta} = 0, D_{T\Delta} = 0$	-148.35	1.047	0.859	0.769	0.660
$C_{RT\Delta} = 0, D_{R\Delta} = 0, D_{T\Delta} = 0$	-127.80	1.025	0.800	0.613	0.490
$C_{RT\Delta} = 0, C_{T\Delta M'} = 0, D_{R\Delta} = 0, D_{T\Delta} = 0$	-123.56	1.151	0.679	0.456	0.000

Having the Landau energy expansions, it is also interesting to investigate the effects of “switching off” some specific couplings by setting their coefficients zero. Fig. 4(b) presents the energy surfaces with respect to the amplitude of Δ_5 and M_5^- modes from the unmodified Landau energy expansion as well as from some examples of modified versions in which some couplings are artificially “switched off”. At each point on the energy surface plots, the R_5^- and T_2 modes have been relaxed at the given amplitudes of Δ_5 and M_5^- modes. We also list in Table IV the energy values and the relative mode amplitudes corresponding to the minimum points of the energy surfaces.

Several interesting features can be seen from Table IV and Fig. 4(b). First, “switching off” any of the trilinear couplings, i.e. $C_{RT\Delta}$ and $C_{T\Delta M'}$, or the cooperative biquadratic couplings, i.e. $D_{R\Delta}$ and $D_{T\Delta}$, reduces the amplitude of the antipolar Δ_5 mode as compared to the unmodified case. This is because all these couplings are associated with the antipolar Δ_5 mode and they are cooperative in nature. Second, when the trilinear coupling term $C_{T\Delta M'}$ is set to zero, the amplitude of the antipolar M_5^- mode will be zero. This is because the M_5^- mode, by itself, is stable in the cubic phase ($A_{M'} > 0$), and its condensation in the $Pbcm$ phase is due entirely to the trilinear coupling $C_{T\Delta M'}$. In addition, from Table

IV, we can see that the R_5^- and T_2 modes always behave in opposite manners, i.e. if one of these two is suppressed, the other one is always enhanced. This is due to the fact that the coupling between the R_5^- and T_2 modes is competitive ($D_{RT} > 0$). Finally, if any of the cooperative coupling terms is “switched off”, the energy of the $Pbcm$ phase (the minimum of the energy surface) will be increased. This means that the $Pbcm$ phase would no more be so low in energy and win over in the competition with other polymorphs such as the $R3c$. All these results demonstrate the crucial role of these cooperative couplings in stabilizing the $Pbcm$ antiferroelectric state.

In summary, we have discussed the characteristics of the Born-Oppenheimer potential energy surface at zero kelvin, explaining why the $Pbcm$ phase, which is a very unusual occurrence in perovskites, exhibits such low energy in ANO. Further research will take temperature-related thermodynamic and kinetic effects into account, so as to better understand how ANO undergoes a complex polymorph evolution process and ultimately stabilizes in the $Pbcm$ phase.

IV. COMPARISONS BETWEEN ANO AND PZO

We have analyzed the mode couplings in ANO, highlighting the crucial role of trilinear and cooperative biquadratic couplings of octahedra rotations and cation antipolar motions in stabilizing the $Pbcm$ antiferroelectric state. In the following, we would like to discuss the similarities and differences between ANO and the prototypical antiferroelectric material PZO in the stabilization mechanisms of their respective $Pbcm$ and $Pbam$ antiferroelectric states. Previously, J. Íñiguez, et al. [28] have provided a detailed elucidation of the mode couplings and the stabilization mechanism for the $Pbam$ antiferroelectric state of PZO. Here, to keep consistency and achieve quantitative comparisons, we briefly reanalyze PZO using the same methodology that we employed for ANO. It should be noted that our results are consistent with the previous literature [28], despite minor differences in methodology.

The room-temperature antiferroelectric state of PZO is the $Pbam$ phase. The dominant symmetry-adapted lattice-distortion modes in the $Pbam$ phase of PZO with respect to its cubic parent phase are [Fig. 5(a)]: (1) R_5^- mode, the $a^-a^-c^0$ octahedra rotations, (2) Σ_2 mode, primarily the antipolar Pb motions $\uparrow\uparrow\downarrow$ and (3) a S_2 mode. These three modes contribute 57.91%, 37.97%, and 3.81% to the total distortion, respectively [Fig. 5(b) and

Table V. Symmetry-adapted lattice-distortion mode decomposition of the $Pbam$ phase of PZO. The structure is obtained by relaxing fully the atomic positions and lattice parameters using GGA-PBEsol functional. The mode amplitudes are reported in the so-called “parent-cell-normalized” values of ISODISTORT.

	R_5^-	Σ_2	S_2	R_4^-	M_5^-	X_1^+
Amplitude (Å)	0.5323	0.4316	0.1366	0.0307	0.0180	0.0179
Percentage (%)	57.91	37.97	3.81	0.19	0.07	0.07

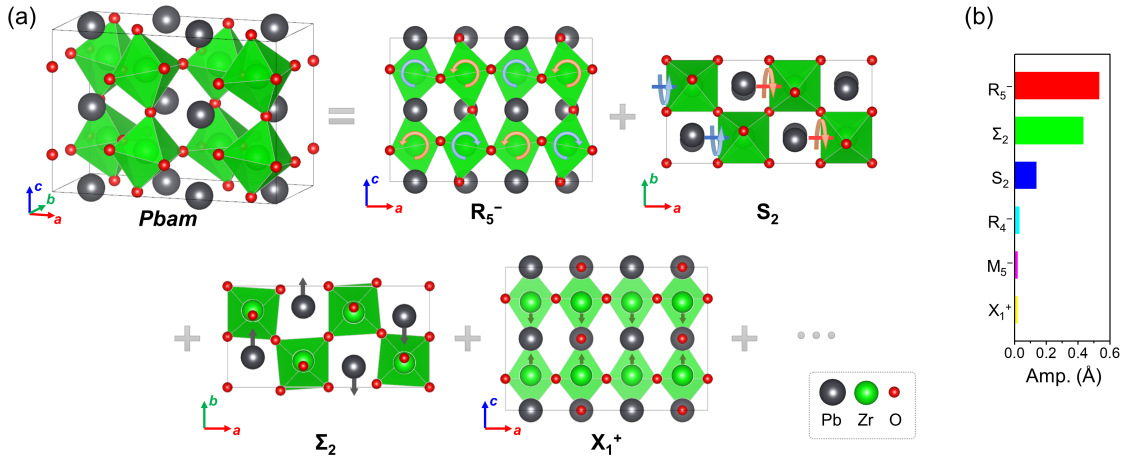


Figure 5. Structure and symmetry-adapted lattice-distortion modes (respect to the cubic reference structure) of PZO in the $Pbam$ phase. (a) Schematics of the $Pbam$ crystal structure and of the lattice-distortion modes of the cubic reference structure contained in the $Pbam$ phase. (b) Mode amplitudes in the $Pbam$ structure, respect to the cubic reference, as optimized with the GGA-PBEsol functional.

Table V]. The S_2 mode has a complex distortion pattern, whose physical interpretation as a modulated oxygen octahedra rotations was recently given by Shapovalov and Stengel [31]. The Landau energy expansion of the $Pbam$ phase of PZO can be written as

$$\begin{aligned}
 E_{Pbam} = & E_{\text{cubic}} + A_R Q_R^2 + B_R Q_R^4 + A_S Q_S^2 + B_S Q_S^4 + A_\Sigma Q_\Sigma^2 + B_\Sigma Q_\Sigma^4 \\
 & + C_{RS\Sigma} Q_R Q_S Q_\Sigma + D_{RS} Q_R^2 Q_S^2 + D_{R\Sigma} Q_R^2 Q_\Sigma^2 + D_{S\Sigma} Q_S^2 Q_\Sigma^2,
 \end{aligned} \tag{4}$$

where Q_R , Q_S , and Q_Σ are the amplitudes of the R_5^- , S_2 , and Σ_2 modes, respectively. Notably, this energy expansion contains a trilinear coupling among the R_5^- , S_2 and Σ_2 modes, and biquadratic couplings between any two of the three modes. It should be kept

in mind that the energy expression has been restricted to the three most dominant modes; there are several other modes in the *Pbam* phase [Fig. 5(b) and Table V], but these modes have been omitted due to their minor amplitudes and negligible energy contributions. We qualified the coefficient values of Eq. (4) by performing a least-squares fitting on a first-principles data set ($R^2 = 0.9952$). The fitted coefficients are summarized in Table VI. We also show in Fig. 6 the energy curves associated with the trilinear and biquadratic couplings of the *Pbam* phase of PZO.

Table VI. Fitted coefficients of the Landau energy expansion of the *Pbam* phase of PZO [Eq. (4)] at fixed cubic lattice parameters. The coefficients are fitted using the units of energy in meV/f.u. and mode amplitudes in Å. The values in brackets are instead the coefficients fitted using relative mode amplitudes (i.e. with mode amplitudes normalized to 1 in the relaxed structure of the *Pbam* phase), which also correspond to the energy contributions (meV/f.u) of the related terms to the energy lowering of this phase. The mode amplitudes in the phase *Pbam* phase can be easily derived from the ratio between the coefficients and the corresponding energy contribution in brackets.

Phase	Fitted coefficients (Energy contributions)			
<i>Pbam</i>	$A_R = -922.6$ (-277.1)	$B_R = +1073.4$ (+96.9)	$C_{RS\Sigma} = -1075.5$ (-38.7)	$D_{R\Sigma} = +1607.3$ (+84.5)
	$A_S = -574.2$ (-14.1)	$B_S = +2205.8$ (+1.3)		$D_{S\Sigma} = +2892.7$ (+12.4)
	$A_\Sigma = -1399.4$ (-244.9)	$B_\Sigma = +2730.6$ (+83.6)		$D_{RS} = +2480.1$ (+18.3)

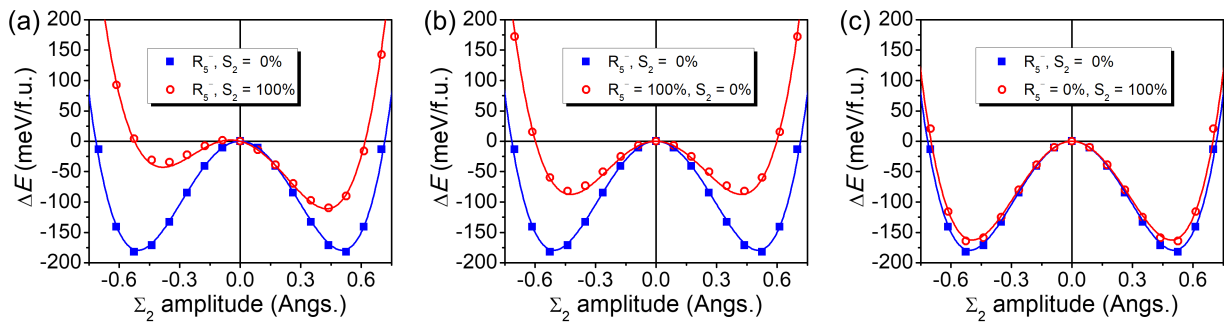


Figure 6. Evolution of the energy of PZO when condensing different symmetry adapted mode in the cubic phase (taken as energy reference) in the absence or eventually in the presence of other modes as indicated by the legends. Mode amplitudes of 100% correspond to the relaxed amplitude in the relaxed *Pbam* phase with cubic lattice parameters.

There is a certain similarity between the *Pbcm* phase of ANO and the *Pbam* phase of

PZO in terms of the mode couplings. First, we note that the trilinear coupling of R_5^- , T_2 and Δ_5 in ANO appears to be similar to the trilinear coupling of R_5^- , S_2 and Σ_2 in PZO: they involve the same $a^-a^-c^0$ octahedra rotations around b -axis in the R_5^- mode, both the T_2 and S_2 can be interpreted as octahedra rotations around c - and a -axis, respectively, modulated along the respective rotation axis direction [31], and both the Δ_5 and Σ_2 consist of b -directed displacements of cations. Second, there is an additional trilinear coupling of T_2 , Δ_5 and M_5^- modes identified in ANO, whose counterpart in the $Pbam$ phase of PZO, despite being overlooked by the energy expansion Eq. (4), is also allowed by symmetry. From symmetry analysis, we identified a trilinear coupling in the $Pbam$ phase of PZO, which involves S_2 , Σ_2 and X_1^+ modes, that is similar to the trilinear coupling of T_2 , Δ_5 and M_5^- in the $Pbcm$ phase of ANO. The X_1^+ mode is also mainly the antipolar motion of cations [Fig. 5(a)], just like the M_5^- mode in the $Pbcm$ phase of ANO. However, due to its negligible amplitude and energy contribution, the X_1^+ mode is usually not considered when constructing the energy expansion. Finally, all the biquadratic coupling terms between any two of the modes are allowed by the symmetry for both $Pbcm$ and $Pbam$. Therefore, from the qualitative perspective, the antiferroelectric $Pbcm$ phase in ANO and $Pbam$ phase in PZO are similar in terms of mode couplings.

Nevertheless, some important differences can be noticed if we inspect more closely the relative mode contributions in the two materials. Among the three most dominant lattice-distortion modes of ANO, the antipolar Δ_5 mode is remarkably less important than the other two modes, the rotational R_5^- and T_2 , as its amplitude and energy contribution are notably smaller. In this sense, the two rotational modes can be considered as the “primary” modes defining the symmetry of the $Pbcm$ phase of ANO, and the antipolar Δ_5 mode as the “secondary” mode whose amplitude and energy contribution are largely enhanced by the coexistence with the primary modes. In PZO, the roles of rotational and antipolar modes are switched: there, the “primary” modes are rotational R_5^- and antipolar Σ_2 , which have larger amplitudes and give significantly larger contributions to the energetics of the $Pbam$ phase, while the remaining rotational S_2 mode is “secondary”. Thus, the antipolar cation motions in the antiferroelectric state of PZO appear to be more dominant than in ANO.

The difference between ANO and PZO lies not only in the relative importance of the antipolar modes with respect to the rotational modes, but also in how these modes interact with each other. The nature of a specific coupling term in the cubic phase, whether it is

cooperative or competitive, can be judged by the sign of the respective coefficient in the energy expansion. However, it is not always straightforward to know the overall coupling effect between any two modes in the strongly distorted low symmetry phase, since multiple coupling terms may be involved. Here, we propose an approach that more thoroughly evaluates the combined impact of all relevant coupling terms, thereby ascertaining the overall coupling effect between any two modes. The detailed derivations are presented in the Appendix. Adopting this approach, we found that in ANO the overall coupling effect of the octahedra rotational modes, i.e. R_5^- and T_2 , on the antipolar Δ_5 mode remain essentially cooperative in the $Pbcm$ phase (calculated based on the energy coefficients listed in Table III and the mode amplitudes $Q_R = 0.4122 \text{ \AA}$, $Q_T = 0.5402 \text{ \AA}$, $Q_\Delta = 0.2230 \text{ \AA}$, $Q_{M'} = 0.0982 \text{ \AA}$):

$$\begin{aligned} \left. \frac{\partial Q_\Delta}{\partial Q_R} \right|_{Pbcm} &= -\frac{C_{RT\Delta}Q_T + 4D_{R\Delta}Q_RQ_\Delta}{2A_\Delta + 12B_\Delta Q_\Delta^2 + 2D_{R\Delta}Q_R^2 + 2D_{T\Delta}Q_T^2} = +0.081 > 0, \\ \left. \frac{\partial Q_\Delta}{\partial Q_T} \right|_{Pbcm} &= -\frac{C_{RT\Delta}Q_R + C_{TM'}Q_{M'} + 4D_{T\Delta}Q_TQ_\Delta}{2A_\Delta + 12B_\Delta Q_\Delta^2 + 2D_{R\Delta}Q_R^2 + 2D_{T\Delta}Q_T^2} = +0.163 > 0. \end{aligned} \quad (5)$$

This can also be evidenced from Figs. 3(a, d, e), where both the first-principles calculation and the energy expansion-based simulation show that the amplitude of the Δ_5 mode is largely enhanced when coexisting with R_5^- or/and T_2 modes. Instead for PZO, by the same analysis, we find that the overall coupling effect of R_5^- and S_2 modes on the antipolar Σ_2 mode remain essentially competitive in the $Pbam$ phase (calculated based on the energy coefficients listed in Table VI and the mode amplitudes $Q_R = 0.5481 \text{ \AA}$, $Q_S = 0.1568 \text{ \AA}$, $Q_\Sigma = 0.4184 \text{ \AA}$):

$$\begin{aligned} \left. \frac{\partial Q_\Sigma}{\partial Q_R} \right|_{Pbam} &= -\frac{C_{RS\Sigma}Q_S + 4D_{R\Sigma}Q_RQ_\Sigma}{2A_\Sigma + 12B_\Sigma Q_\Sigma^2 + 2D_{R\Sigma}Q_R^2 + 2D_{S\Sigma}Q_S^2} = -0.323 < 0, \\ \left. \frac{\partial Q_\Sigma}{\partial Q_S} \right|_{Pbam} &= -\frac{C_{RS\Sigma}Q_R + 4D_{S\Sigma}Q_SQ_\Sigma}{2A_\Sigma + 12B_\Sigma Q_\Sigma^2 + 2D_{R\Sigma}Q_R^2 + 2D_{S\Sigma}Q_S^2} = -0.042 < 0. \end{aligned} \quad (6)$$

As can be seen from Fig. 6, coexistence with the R_5^- or/and S_2 modes suppresses the amplitude of the Σ_2 mode.

To summarize, although very similar antipolar and octahedra rotation modes – trilinearly coupled by symmetry – are involved in both cases, we find a slightly different story in ANO and PZO. In ANO, the antipolar Δ_5 mode by itself only shows a weak instability, in contrast with the strong instability of the antipolar Σ_2 mode in PZO. The emergence of the Δ_5 mode in the antiferroelectric $Pbcm$ phase of ANO is at first favored by the trilinear coupling

with the rotational R_5^- and T_2 modes. This behavior reminds us of the concept of hybrid-improper ferroelectricity [45–47], and suggests a more hybrid-improper-like nature of the antipolar cation motions in ANO [48]. Then, this Δ_5 mode is also significantly enhanced by cooperative biquadratic couplings with R_5^- and T_2 modes, which corresponds to a so-called triggered mechanism [49]. In comparison, the Σ_2 antipolar cation motions in PZO appear more proper and compete with R_5^- and S_2 modes. This observation highlights the importance of octahedra rotations in inducing the cation antipolar motions in ANO. Usually, the octahedra rotations can be tuned by various factors such as strain, pressure, doping, defects, etc [50–53]. In this regard, investigating the control of octahedra rotations so as to modulate the AFE property in ANO will also be an interesting perspective for a future work.

V. CONCLUSIONS

In this study, we have emphasized the crucial role of trilinear and biquadratic couplings of octahedra rotations and cation antipolar motions in stabilizing the $Pbcm$ phase in ANO. These anharmonic couplings contribute significantly to lower the energy, making the $Pbcm$ phase energetically more favorable compared to other competing variants. We have also conducted a comparative discussion between the antiferroelectric phases of ANO and PZO, which are distinct but similarly combine antipolar and octahedra rotation motions trilinearly coupled by symmetry. Unlike in the $Pbam$ phase of PZO, the antipolar motions in $Pbcm$ phase of ANO appear to be secondary. Their significant amplitude in the $Pbcm$ phase arises from the combination of hybrid-improper (i.e. trilinear coupling with primary octahedra rotations) and triggered (i.e. cooperative biquadratic coupling with primary octahedra rotations) mechanisms. This contrasts with PZO in which antipolar motions are primary and compete with octahedra rotations.

ACKNOWLEDGMENTS

This work was supported by the European Union’s Horizon 2020 research and innovation program under grant agreement No. 964931 (TSAR) and by F.R.S.-FNRS Belgium under PDR grant T.0107.20 (PROMOSPAN). H.Z. acknowledges the International Postdoctoral

Exchange Fellowship (PC2020060) and the Research IPD-STEMA Program. S.A. acknowledges Erasmus+International Credit Mobility program 2023 of Université de Liège and the PRD-CCD ARES 2019-2024 project: *Le coltan du Kivu: Capacité de traitement physico-chimique et études d'applications* (Grant No. 32210). The authors acknowledge the use of the CECI supercomputer facilities funded by the F.R.S-FNRS (Grant No. 2.5020.1) and of the Tier-1 supercomputer of the Fédération Wallonie-Bruxelles funded by the Walloon Region (Grant No. 1117545).

APPENDIX: EVALUATION OF OVERALL COUPLING EFFECT BETWEEN DISTORTION MODES

Having the energy expansion and the related coefficients, it is relatively easy to judge from the sign of the coefficients of specific coupling terms which modes are initially competitive or cooperative in the cubic reference. However, it is not always so straightforward to determine the overall coupling effect between different modes in the low-energy phases, especially when multiple coupling terms are involved. In this Appendix, we present an approach to comprehensively assess the whole effect of all relevant coupling terms, thereby evaluate the overall impact of one mode on the other.

Let us consider a typical example in a relatively general sense, where three modes P , Q_1 and Q_2 are mutually coupled and the energy expansion is given by

$$E = E_0 + AP^2 + BP^4 + CQ_1Q_2P + D_1Q_1^2P^2 + D_2Q_2^2P^2, \quad (7)$$

where A , B , C , D_1 and D_2 are energy coefficients, and E_0 includes all the energy contributions irrelevant to P . This energy expansion contains one trilinear coupling term, and two biquadratic terms. The goal is to reveal how P will be affected if small perturbation is applied on Q_1 or Q_2 near the energy minimum point.

The P_0 (the relaxed value of P at given Q_1 and Q_2) minimizes the energy and must satisfy the condition $\frac{\partial E}{\partial P}|_{P_0} = 0$, which yields

$$2AP_0 + 4BP_0^3 + CQ_1Q_2 + 2D_1Q_1^2P_0 + 2D_2Q_2^2P_0 = 0. \quad (8)$$

This equation gives an implicit expression of the function $P_0 = P_0(Q_1, Q_2)$. Taking the partial derivatives with respect to Q_1 and Q_2 , respectively, on both side of Eq. (8), we have

$$\begin{aligned}
2A \frac{\partial P_0}{\partial Q_1} + 12BP_0^2 \frac{\partial P_0}{\partial Q_1} + CQ_2 + 4D_1Q_1P_0 + 2D_1Q_1^2 \frac{\partial P_0}{\partial Q_1} + 2D_2Q_2^2 \frac{\partial P_0}{\partial Q_1} &= 0, \\
2A \frac{\partial P_0}{\partial Q_2} + 12BP_0^2 \frac{\partial P_0}{\partial Q_2} + CQ_1 + 2D_1Q_1^2 \frac{\partial P_0}{\partial Q_2} + 4D_2Q_2P_0 + 2D_2Q_2^2 \frac{\partial P_0}{\partial Q_2} &= 0.
\end{aligned} \tag{9}$$

Solving $\frac{\partial P_0}{\partial Q_1}$ and $\frac{\partial P_0}{\partial Q_2}$ from Eq. (9), and evaluating at the energy minimum point (denoted as “min E ”, where $P_0 = P_{00}$, $Q_1 = Q_{10}$, $Q_2 = Q_{20}$), we can get

$$\begin{aligned}
\left. \frac{\partial P_0}{\partial Q_1} \right|_{\min E} &= -\frac{CQ_{20} + 4D_1Q_{10}P_{00}}{2A + 12BP_{00}^2 + 2D_1Q_{10}^2 + 2D_2Q_{20}^2}, \\
\left. \frac{\partial P_0}{\partial Q_2} \right|_{\min E} &= -\frac{CQ_{10} + 4D_2Q_{20}P_{00}}{2A + 12BP_{00}^2 + 2D_1Q_{10}^2 + 2D_2Q_{20}^2}.
\end{aligned} \tag{10}$$

The partial derivatives of P_0 with respect to Q_1 and Q_2 provide the evaluation of the overall impact of Q_1 and Q_2 on P at the energy minimum point, respectively, with a positive value meaning a cooperative effect, and negative meaning competitive.

In the specific case of ANO, replacing P by Q_Δ , Q_1 by Q_R , and Q_2 by Q_T and considering an additional term $C_{T\Delta M}Q_TQ_\Delta Q_M$ in the energy expansion of the $Pbcm$ phase of ANO, Eq. (5) can be derived following the same procedure.

In the specific case of PZO, replacing P by Q_Σ , Q_1 by Q_R , and Q_2 by Q_S , Eq. (10) is directly turned into Eq. (6).

As a final remark, we point out that the equations can be further simplified if the mode amplitudes are relatively evaluated (renormalized so as to make $P'_{00} = Q'_{10} = Q'_{20} = 1$ at the energy minimum point):

$$\begin{aligned}
\left. \frac{\partial P'_0}{\partial Q'_1} \right|_{\min E} &= -\frac{C' + 4D'_1}{2A' + 12B' + 2D'_1 + 2D'_2}, \\
\left. \frac{\partial P'_0}{\partial Q'_2} \right|_{\min E} &= -\frac{C' + 4D'_2}{2A' + 12B' + 2D'_1 + 2D'_2},
\end{aligned} \tag{11}$$

where the primed coefficients have the physical meaning of their respective energy contributions in the studied phase (corresponding to the values in parentheses in Tabs. III, VI). In cases where only the qualitative nature of the coupling effect is of concern, rather than its quantitative strength, this simplified form is easier to use. We notice that using such

primed equivalent to Eq. (5) and (6) would not change our conclusions.

- [1] Clive A. Randall, Zhongming Fan, Ian Reaney, Long-Qing Chen, and Susan Trolier-McKinstry. Antiferroelectrics: History, fundamentals, crystal chemistry, crystal structures, size effects, and applications. *Journal of the American Ceramic Society*, 104(8):3775–3810, 2021.
- [2] Karin M. Rabe. *Antiferroelectricity in Oxides: A Reexamination*. In *Functional Metal Oxides* (eds S.B. Ogale, T.V. Venkatesan and M.G. Blamire), pages 221–244. John Wiley & Sons, Ltd, 2013.
- [3] Xiaoli Tan, Cheng Ma, Joshua Frederick, Sarah Beckman, and Kyle G. Webber. The antiferroelectric \leftrightarrow ferroelectric phase transition in lead-containing and lead-free perovskite ceramics. *Journal of the American Ceramic Society*, 94(12):4091–4107, 2011.
- [4] Xihong Hao, Jiwei Zhai, Ling Bing Kong, and Zhengkui Xu. A comprehensive review on the progress of lead zirconate-based antiferroelectric materials. *Progress in Materials Science*, 63:1–57, 2014.
- [5] Zhen Liu, Teng Lu, Jiaming Ye, Genshui Wang, Xianlin Dong, Ray Withers, and Yun Liu. Antiferroelectrics for energy storage applications: A review. *Advanced Materials Technologies*, 3(9):1800111, 2018.
- [6] Pablo Vales-Castro, Romain Faye, Miquel Vellvehi, Youri Nouchokgwe, Xavier Perpiñà, J. M. Caicedo, Xavier Jordà, Krystian Roleder, Dariusz Kajewski, Amador Perez-Tomas, Emmanuel Defay, and Gustau Catalan. Origin of large negative electrocaloric effect in antiferroelectric PbZrO_3 . *Physical Review B*, 103(5):054112, 2021.
- [7] Desheng Fu, Makoto Endo, Hiroki Taniguchi, Tomoyasu Taniyama, and Mitsuru Itoh. AgNbO_3 : A lead-free material with large polarization and electromechanical response. *Applied Physics Letters*, 90(25):252907, 2007.
- [8] Ye Tian, Li Jin, Hangfeng Zhang, Zhuo Xu, Xiaoyong Wei, E. D. Politova, S. Yu Stefanovich, Nadezda V. Tarakina, Isaac Abrahams, and Haixue Yan. High energy density in silver niobate ceramics. *Journal of Materials Chemistry A*, 4(44):17279–17287, 2016.
- [9] Lei Zhao, Qing Liu, Jing Gao, Shujun Zhang, and Jing-Feng Li. Lead-free antiferroelectric silver niobate tantalate with high energy storage performance. *Advanced Materials*, 29(31):1701824, 2017.

- [10] Li-Feng Zhu, Shiqing Deng, Lei Zhao, Gen Li, Qi Wang, Linhai Li, Yongke Yan, He Qi, Bo-Ping Zhang, Jun Chen, and Jing-Feng Li. Heterovalent-doping-enabled atom-displacement fluctuation leads to ultrahigh energy-storage density in AgNbO_3 -based multilayer capacitors. *Nature Communications*, 14(1):1166, 2023.
- [11] Jing Gao, Qian Li, Shujun Zhang, and Jing-Feng Li. Lead-free antiferroelectric AgNbO_3 : Phase transitions and structure engineering for dielectric energy storage applications. *Journal of Applied Physics*, 128(7):070903, 2020.
- [12] Dong Yang, Jing Gao, Liang Shu, Yi-Xuan Liu, Jingru Yu, Yuanyuan Zhang, Xuping Wang, Bo-Ping Zhang, and Jing-Feng Li. Lead-free antiferroelectric niobates AgNbO_3 and NaNbO_3 for energy storage applications. *Journal of Materials Chemistry A*, 8(45):23724–23737, 2020.
- [13] Ye Tian, Panpan Song, Giuseppe Viola, Jindou Shi, Jing Li, Li Jin, Qingyuan Hu, Yonghao Xu, Wanyin Ge, Zhongna Yan, Dou Zhang, Nadezda V. Tarakina, Isaac Abrahams, Xiaoyong Wei, and Haixue Yan. Silver niobate perovskites: Structure, properties and multifunctional applications. *Journal of Materials Chemistry A*, 10(28):14747–14787, 2022.
- [14] M. Łukaszewski, M. Pawełczyk, J. Hańderek, and A. Kania. On the phase transitions in silver niobate AgNbO_3 . *Phase Transitions*, 3(3):247–257, 1983.
- [15] A. Kania and J. Kwapulinski. $\text{Ag}_{1-x}\text{Na}_x\text{NbO}_3$ (ANN) solid solutions: From disordered antiferroelectric AgNbO_3 to normal antiferroelectric NaNbO_3 . *Journal of Physics: Condensed Matter*, 11(45):8933–8946, 1999.
- [16] Jan Fabry, Zdenek Zikmund, Antoni Kania, and Vaclav Petricek. Silver niobium trioxide, AgNbO_3 . *Acta Crystallographica Section C*, 56(8):916–918, 2000.
- [17] Ph Sciau, A. Kania, B. Dkhil, E. Suard, and A. Ratuszna. Structural investigation of AgNbO_3 phases using X-ray and neutron diffraction. *Journal of Physics: Condensed Matter*, 16(16):2795–2810, 2004.
- [18] Igor Levin, Victor Krayzman, Joseph C. Woicik, Jenia Karapetrova, Thomas Proffen, Matthew G. Tucker, and Ian M. Reaney. Structural changes underlying the diffuse dielectric response in AgNbO_3 . *Physical Review B*, 79(10):104113, 2009.
- [19] Ye Tian, Jing Li, Qingyuan Hu, Li Jin, Kun Yu, Jinglei Li, E. D. Politova, S. Yu Stefanovich, Zhuo Xu, and Xiaoyong Wei. Ferroelectric transitions in silver niobate ceramics. *Journal of Materials Chemistry C*, 7(4):1028–1034, 2019.
- [20] A. Kania, K. Roleder, and M. Łukaszewski. The ferroelectric phase in AgNbO_3 . *Ferroelectrics*,

- 52(1):265–269, 1983.
- [21] Hiroki Moriwake, Craig A. J. Fisher, Akihide Kuwabara, and Desheng Fu. First-principles study of point defect formation in AgNbO_3 . *Japanese Journal of Applied Physics*, 52(9S1):09KF08, 2013.
- [22] Masatomo Yashima, Shota Matsuyama, Rikiya Sano, Mitsuru Itoh, Kenji Tsuda, and Desheng Fu. Structure of ferroelectric silver niobate AgNbO_3 . *Chemistry of Materials*, 23(7):1643–1645, 2011.
- [23] Hiroki Moriwake, Craig A. J. Fisher, Akihide Kuwabara, and Desheng Fu. A first-principles study of the ferroelectric phase of AgNbO_3 . *Japanese Journal of Applied Physics*, 51:09LE02, 2012.
- [24] C J Howard, R L Withers, K S Knight, and Z Zhang. $(\text{Ca}_{0.37}\text{Sr}_{0.63})\text{TiO}_3$ perovskite—an example of an unusual class of tilted perovskites. *Journal of Physics: Condensed Matter*, 20(13):135202, 2008.
- [25] Safari Amisi, Philippe Lambin, and Philippe Ghosez. Structural and dynamical phase transitions of NaNbO_3 from first-principles calculations. *Phys. Rev. Mater.*, 7:024408, 2023.
- [26] Michael W. Lufaso and Patrick M. Woodward. Prediction of the crystal structures of perovskites using the software program SPUDS. *Acta Crystallographica Section B*, 57(6):725–738, 2001.
- [27] Nicole A. Benedek and Craig J. Fennie. Why are there so few perovskite ferroelectrics? *The Journal of Physical Chemistry C*, 117(26):13339–13349, 2013.
- [28] Jorge Íñiguez, Massimiliano Stengel, Sergey Prosandeev, and L. Bellaiche. First-principles study of the multimode antiferroelectric transition in PbZrO_3 . *Phys. Rev. B*, 90:220103, 2014.
- [29] J. Hlinka, T. Ostapchuk, E. Buixaderas, C. Kadlec, P. Kuzel, I. Gregora, J. Kroupa, M. Savinov, A. Klic, J. Drahokoupil, I. Etxebarria, and J. Dec. Multiple soft-mode vibrations of lead zirconate. *Physical Review Letters*, 112(19):197601, 2014.
- [30] Safari Amisi. Ab initio investigation in PbZrO_3 antiferroelectric: Structural and vibrational properties. *The European Physical Journal Plus*, 136(6):653, 2021.
- [31] Konstantin Shapovalov and Massimiliano Stengel. Tilt-driven antiferroelectricity in PbZrO_3 . *Physical Review Materials*, 7:L071401, 2023.
- [32] Xavier Gonze, Bernard Amadon, Gabriel Antonius, Frédéric Arnardi, Lucas Baguet, Jean-Michel Beuken, Jordan Bieder, François Bottin, Johann Bouchet, Eric Bousquet, Nils Brouwer,

- Fabien Bruneval, Guillaume Brunin, Théo Cavignac, Jean-Baptiste Charraud, Wei Chen, Michel Côté, Stefaan Cottenier, Jules Denier, Grégory Geneste, Philippe Ghosez, Matteo Giantomassi, Yannick Gillet, Olivier Gingras, Donald R. Hamann, Geoffroy Hautier, Xu He, Nicole Helbig, Natalie Holzwarth, Yongchao Jia, François Jollet, William Lafargue-Dit-Hauret, Kurt Lejaeghere, Miguel A. L. Marques, Alexandre Martin, Cyril Martins, Henrique P. C. Miranda, Francesco Naccarato, Kristin Persson, Guido Petretto, Valentin Planes, Yann Pouillon, Sergei Prokhorenko, Fabio Ricci, Gian-Marco Rignanese, Aldo H. Romero, Michael Marcus Schmitt, Marc Torrent, Michiel J. van Setten, Benoit Van Troeye, Matthieu J. Verstraete, Gilles Zérah, and Josef W. Zwanziger. The ABINIT project: Impact, environment and recent developments. *Computer Physics Communications*, 248:107042, 2020.
- [33] X. Gonze, F. Jollet, F. Abreu Araujo, D. Adams, B. Amadon, T. Applencourt, C. Audouze, J.-M. Beuken, J. Bieder, A. Bokhanchuk, E. Bousquet, F. Bruneval, D. Caliste, M. Côté, F. Dahm, F. Da Pieve, M. Delaveau, M. Di Gennaro, B. Dorado, C. Espejo, G. Geneste, L. Genovese, A. Gerossier, M. Giantomassi, Y. Gillet, D.R. Hamann, L. He, G. Jomard, J. Laflamme Janssen, S. Le Roux, A. Levitt, A. Lherbier, F. Liu, I. Lukačević, A. Martin, C. Martins, M.J.T. Oliveira, S. Poncé, Y. Pouillon, T. Rangel, G.-M. Rignanese, A.H. Romero, B. Rousseau, O. Rubel, A.A. Shukri, M. Stankovski, M. Torrent, M.J. Van Setten, B. Van Troeye, M.J. Verstraete, D. Waroquiers, J. Wiktor, B. Xu, A. Zhou, and J.W. Zwanziger. Recent developments in the ABINIT software package. *Computer Physics Communications*, 205:106–131, 2016.
- [34] X. Gonze, B. Amadon, P.-M. Anglade, J.-M. Beuken, F. Bottin, P. Boulanger, F. Bruneval, D. Caliste, R. Caracas, M. Côté, T. Deutsch, L. Genovese, Ph. Ghosez, M. Giantomassi, S. Goedecker, D.R. Hamann, P. Hermet, F. Jollet, G. Jomard, S. Leroux, M. Mancini, S. Mazevet, M.J.T. Oliveira, G. Onida, Y. Pouillon, T. Rangel, G.-M. Rignanese, D. Sangalli, R. Shaltaf, M. Torrent, M.J. Verstraete, G. Zerah, and J.W. Zwanziger. ABINIT: First-principles approach to material and nanosystem properties. *Computer Physics Communications*, 180(12):2582–2615, 2009.
- [35] X. Gonze, J.-M. Beuken, R. Caracas, F. Detraux, M. Fuchs, G.-M. Rignanese, L. Sindic, M. Verstraete, G. Zerah, F. Jollet, M. Torrent, A. Roy, M. Mikami, Ph. Ghosez, J.-Y. Raty, and D.C. Allan. First-principles computation of material properties: The ABINIT software project. *Computational Materials Science*, 25(3):478–492, 2002.

- [36] John P. Perdew, Adrienn Ruzsinszky, Gábor I. Csonka, Oleg A. Vydrov, Gustavo E. Scuseria, Lucian A. Constantin, Xiaolan Zhou, and Kieron Burke. Restoring the density-gradient expansion for exchange in solids and surfaces. *Physical Review Letters*, 100:136406, 2008.
- [37] M.J. van Setten, M. Giantomassi, E. Bousquet, M.J. Verstraete, D.R. Hamann, X. Gonze, and G.-M. Rignanese. The PseudoDojo: Training and grading a 85 element optimized norm-conserving pseudopotential table. *Computer Physics Communications*, 226:39–54, 2018.
- [38] D. R. Hamann. Optimized norm-conserving Vanderbilt pseudopotentials. *Physical Review B*, 88(8):085117, August 2013.
- [39] John P. Perdew and Yue Wang. Accurate and simple analytic representation of the electron-gas correlation energy. *Phys. Rev. B*, 45:13244–13249, 1992.
- [40] Xavier Gonze and Changyol Lee. Dynamical matrices, Born effective charges, dielectric permittivity tensors, and interatomic force constants from density-functional perturbation theory. *Physical Review B*, 55(16):10355–10368, 1997.
- [41] Branton J. Campbell, Harold T. Stokes, David E. Tanner, and Dorian M. Hatch. ISODISPLACE: a web-based tool for exploring structural distortions. *Journal of Applied Crystallography*, 39(4):607–614, 2006.
- [42] Dorian M. Hatch and Harold T. Stokes. INVARIANTS: program for obtaining a list of invariant polynomials of the order-parameter components associated with irreducible representations of a space group. *Journal of Applied Crystallography*, 36:951–952, 2003.
- [43] A. Glazer. The classification of tilted octahedra in perovskites. *Acta Crystallographica Section B*, 28(11):3384–3392, 1972.
- [44] Andrew T. Mulder, Nicole A. Benedek, James M. Rondinelli, and Craig J. Fennie. Turning ABO_3 antiferroelectrics into ferroelectrics: Design rules for practical rotation-driven ferroelectricity in double perovskites and $\text{A}_3\text{B}_2\text{O}_7$ ruddlesden-popper compounds. *Advanced Functional Materials*, 23(38):4810–4820, 2013.
- [45] Eric Bousquet, Matthew Dawber, Nicolas Stucki, Céline Lichtensteiger, Patrick Hermet, Stefano Gariglio, Jean-Marc Triscone, and Philippe Ghosez. Improper ferroelectricity in perovskite oxide artificial superlattices. *Nature*, 452(7188):732–736, 2008.
- [46] Nicole A. Benedek and Craig J. Fennie. Hybrid improper ferroelectricity: A mechanism for controllable polarization-magnetization coupling. *Physical Review Letters*, 106(10):107204, 2011.

- [47] Nicole A. Benedek and Michael A. Hayward. Hybrid improper ferroelectricity: A theoretical, computational, and synthetic perspective. *Annual Review of Materials Research*, 52(1):331–355, 2022.
- [48] L. Bellaiche and Jorge Íñiguez. Universal collaborative couplings between oxygen-octahedral rotations and antiferroelectric distortions in perovskites. *Physical Review B*, 88(1):014104, 2013.
- [49] Philippe Ghosez and Javier Junquera. Modeling of ferroelectric oxide perovskites: From first to second principles. *Annual Review of Condensed Matter Physics*, 13(1):325–364, 2022.
- [50] Thomas Angsten and Mark Asta. Epitaxial phase diagrams of SrTiO₃, CaTiO₃, and SrHfO₃: Computational investigation including the role of antiferrodistortive and *A*-site displacement modes. *Physical Review B*, 97(13):134103, 2018.
- [51] Muhtar Ahart, Maddury Somayazulu, R. E. Cohen, P. Ganesh, Przemyslaw Dera, Ho-kwang Mao, Russell J. Hemley, Yang Ren, Peter Liermann, and Zhigang Wu. Origin of morphotropic phase boundaries in ferroelectrics. *Nature*, 451(7178):545–548, 2008.
- [52] Yajun Zhang, Jie Wang, and Philippe Ghosez. Unraveling the suppression of oxygen octahedra rotations in A₃B₂O₇ Ruddlesden-Popper compounds: Engineering multiferroicity and beyond. *Physical Review Letters*, 125(15):157601, 2020.
- [53] Jiahui Jia, Xu He, Arsalan Akhtar, Gervasi Herranz, and Miguel Pruneda. Dynamic control of octahedral rotation in perovskites by defect engineering. *Physical Review B*, 105(22):224112, 2022.